KSME

Springer

Journal of Mechanical Science and Technology 38 (7) 2024

Original Article
DOI 10.1007/s12206-024-0650-7

Keywords:
· Clamping pressure
· Ohmic resistance
· Polymer electrolyte fuel cell
· Stiffened rib
· Rib-stiffened channel
· Structural analysis
· Computational fluid dynamics

Correspondence to:
Youngseung Na
ysna@uos.ac.kr

Citation:
Kim, C., Im, S., Na, Y. (2024). Robust channel structures of proton exchange membrane fuel cells for uniform clamping pressure to gas diffusion layers. Journal of Mechanical Science and Technology 38 (7) (2024) 3817~3827.
http://doi.org/10.1007/s12206-024-0650-7

Received November 5th, 2023
Revised March 5th, 2024
Accepted March 16th, 2024

† Recommended by Editor
Tong Seop Kim

Robust channel structures of proton exchange membrane fuel cells for uniform clamping pressure to gas diffusion layers

Choeun Kim, Seongsu Im and Youngseung Na

Department of Mechanical and Information Engineering, University of Seoul, Seoul, Korea

Abstract Proton exchange membrane fuel cells (PEMFCs) not only provide rapid dynamic response but also operate at low temperatures, which are desirable characteristics for transportation applications. However, metal bipolar plates in PEMFCs often deform under excessive clamping pressure, resulting in uneven pressure distribution. Rib-stiffened channels have been proposed to increase the structural stiffness of the bipolar plates, promoting durability. Parametric studies reveal that the supporting walls formed by the rib structure and a reduced top surface area contribute to better resistance against clamping force. Structural analysis and experimental assessments have confirmed the effectiveness of rib-stiffened channels in mitigating deformation. To ensure uniform compression of the gas diffusion layer during bolt assembly, a combined straight and rib-stiffened flow field has been designed and validated through structural simulations. Rib structures do not compromise fuel cell performance, as proved by computational fluid dynamics simulation with electrochemical reaction.

1. Introduction

Greenhouse gas emissions need to be reduced to mitigate the impact of global warming [1]. Recent studies have suggested that battery electric cars alone may not be sufficient to achieve this goal, particularly for heavy-duty and long-range applications [2]. Hydrogen has a higher storage capacity per unit mass than batteries, making it a potential alternative for heavy-duty vehicles [3]. Proton exchange membrane fuel cells (PEMFCs) are the common type of fuel cells used in transportation applications because of their rapid dynamic response and low operating temperatures [4]. PEMFCs also have high power density, indicating that they can produce a large amount of power depending on their size and weight; this is important for transportation applications.

PEMFCs consist of several components, including bipolar plates (BPs), membrane electrode assemblies (MEAs), gas diffusion layers (GDLs) and sealants. BPs separate the reactions occurring at the anode and cathode. The hydrogen oxidation reaction occurs at the anode, as expressed in Eq. (1), and the water production reaction occurs at the cathode, as expressed in Eq. (2).

$$\text{Anode}: H_2 \rightarrow 2H^+ + 2e^- \tag{1}$$

$$\text{Cathode}: 2H^+ + 2e^- + \frac{1}{2}O^2 \rightarrow H_2O\,. \tag{2}$$

BPs are typically made of either graphite or other metals. Each material is used depending on the specific application and performance requirements. Graphite BPs are widely used in stationary applications such as household power generation because they do not have strict restrictions on volume and shape [5, 6]. However, metal BPs are widely used in automotive applications to overcome the disadvantages of graphite BPs that are bulky and fragile [7]. Thin metal BPs are imperative to minimize the overall stack weight for mobile applications that are

manufactured by forming processes, such as stamping and hydroforming [8]. After stamping or hydroforming, the metal BPs in the stack continue to deform because of the clamping force. This deformation is a significant problem when replacing metal BPs for maintenance purposes, thereby exerting a substantial influence on cell-to-cell variations.

To reduce the weight of the thin metal plate to a minimum and prevent it from being deformed, a method of uniformly applying the entire clamping pressure was devised. By pre-deforming the end plate in the opposite direction, the issue of insufficient force application at the center was resolved, ensuring uniform pressure distribution throughout [9]. Several strategies have been presented to obtain uniform and optimal contact pressure distribution. One approach to achieving pressure uniformity involves designing end plates. Lee et al. proposed a pre-curved end plate design to yield a uniform pressure to the fuel cell stack [10]. Topology optimized end plates were suggested to maximize the structural rigidity and uniformize the pressure distribution [11].

Another approach involves designing BPs. While maintaining the structural strength, BPs are made of light aluminum metals. However, aluminum degrades fuel cell performance owing to metal ions. To prevent corrosion, coating or alloying methods are employed, thereby increasing the material cost [12]. The forming process can affect the stiffness of metal sheets [13]. Among the forming processes, etching of metal plates is also possible but not sufficiently thin to make metal sheets [14]. Most economical and suitable forming methods are hydroforming [15] or stamping [16]. The annealing process can harden metal sheets [17].

Because both forming processes use a corrugated pattern, forming a complex-shaped flow field is difficult. Consequently, parallel flow fields are commonly employed in transportation applications. Parallel flow fields not only address the complexity issue, but also contribute to reducing the pressure drop, thereby minimizing the overall power consumption by employing blowers instead of compressors. However, a simple parallel structure can be deformed owing to excessive clamping pressure, leading to an uneven pressure distribution in the GDLs [18]. Excessive clamping pressure can hinder gas diffusion in the GDL; however, insufficient pressure induces high contact resistance.

This study aims to strengthen the structural stiffness of BPs to ensure uniform compression of GDLs and increase stack power density by reducing the weight of the BPs. Parametric studies were conducted by modifying the geometries of rib structures in straight channels. A comparative analysis of deformation in straight and rib-stiffened BPs was performed through structural analysis and experimentation, validating the improvement in structural stiffness. Bolt assembly simulations were conducted to achieve uniform distribution during assembly, utilizing both straight and rib-stiffened combined flow fields. The primary objective of this work is to increase the structural stiffness of the BPs, while considering its potential impact on the electrochemical performance of the fuel cell. Consequently, electrochemical simulations were performed to confirm that the rib-stiffened flow field does not have a detrimental impact on fuel cell performance.

2. Materials and methods

2.1 Computational finite element analysis

Stress and reaction forces were analyzed using metal BP models. To strengthen the structural stiffness of the BP channels, the structure of the rib-stiffened channels changed with the parameters, as shown in Fig. 1. The height (H) is the distance from the top of the flow field to the bottom of the stiffened rib, and width (W) is the shifting distance from the original channel position. The rib length (L) is the indented part, and the distance (D) is the gap between the ribs. Table 1 lists the geometric parameters considered at each variable level. First, the height of the ribs was changed, while retaining the other parameters. The purpose of this simulation was to study the effects of the rib height on the deformation of BPs. After conducting the first parametric study, the height of the ribs was fixed, and the number of ribs was altered by adjusting their distance and length. Each channel had an identical distance and length.

Table 1. Geometric dimensions of rib structures in rib-stiffened channels for PEMFCs.

	Dimension (mm)
Distance between ribs (D)	2, 3, 4, 6
Rib length (L)	2, 3, 4, 6
Rib height (H)	0.2, 0.4
Rib width (W)	0.2, 0.3

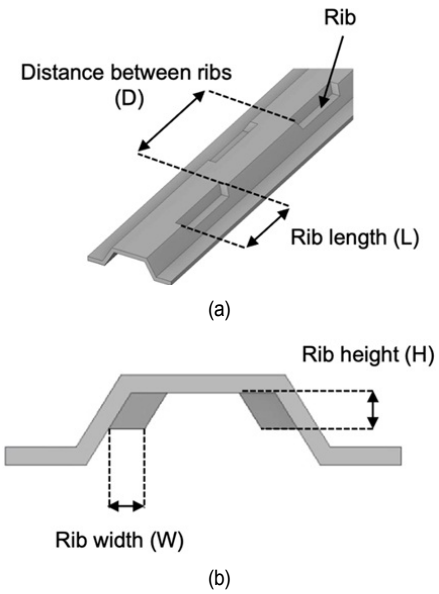

Fig. 1. Geometric parameters of a rib-stiffened channel for PEMFCs: (a) perspective view showing rib spacing (D) and length (L); (b) cross-sectional view highlighting rib width (W) and height (H).

Next, the ratio of the rib length to the distance between ribs was varied by maintaining the number of ribs and height constant while changing the ratio between the length of the ribs and the distance between them. The final parametric study involved changing the width of the ribs while maintaining the other parameters constant. These parametric studies were conducted to investigate the effects of different rib geometries on the structural characteristics of the channel.

Two BP designs shown in Fig. 2(a) straight, and Fig. 2(b) rib-stiffened parallel channel design were simulated and compared with experimental results. Deformation of the BP during compression was observed and compared with the experimental data. To investigate the impact of BP design on GDL compression when using bolts, two BP designs shown in Fig. 2(a) straight and Fig. 2(b) combined straight and rib-stiffened channel design were simulated. To compare the contact resistance resulting from GDL compression, both GDL deformation and stress were measured. Highly compressed GDL shows lower contact resistance [19]. The overall area of the BP was 43.2×33.6 mm^2, along with an active area of 30×30 mm^2. The channel shape is based on the BP design proposed by Peng et al. [20]. Both the BPs had the same channel cross-sectional geometry, as shown in Fig. 2(d). The fillet radius was not considered in the analysis owing to its negligible effect on the pressure distribution.

Commercial software ANSYS Mechanical 2021 R1 was used for the static structural analysis based on the finite element method (FEM). Fig. 3(a) is segmented channel used for the parametric study, including the cathode BP, anode BP, coolant gasket and endplates. Fig. 3(b) illustrates the boundary condi-

Table 2. Material properties of components used in structural analysis.

Component	Bipolar plate	Gasket	GDL
Material	Stainless steel	Silicon rubber	Carbon paper
Young's modulus (MPa)	193000	15.91	6.3
Poisson's ratio	0.31	0.49	0.09
Reference	[21]	[22]	[23]

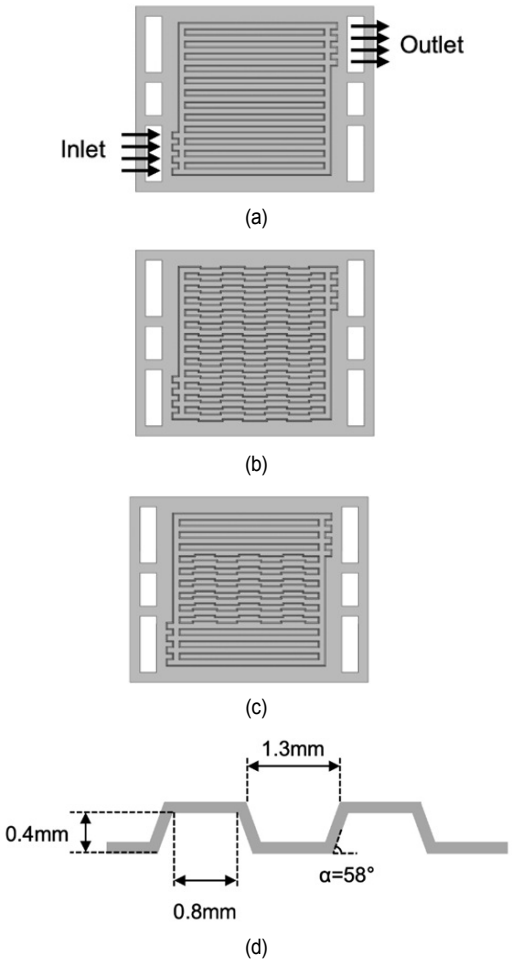

Fig. 2. Schematic of cathode bipolar plate for PEMFCs showing a parallel flow field with (a) straight; (b) rib-stiffened; (c) combined straight and rib-stiffened channels; (d) detailed cross-sectional dimensions of the channels.

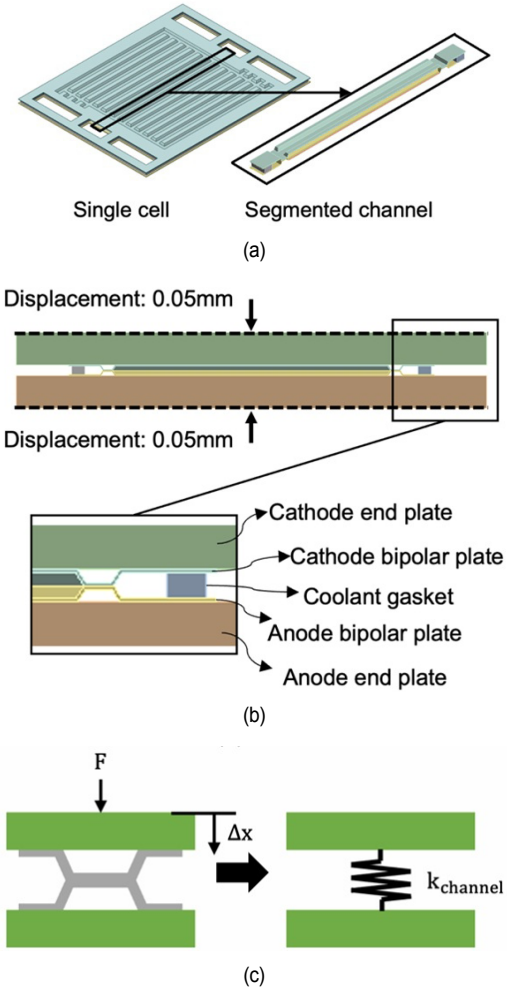

Fig. 3. Finite element analysis model for PEMFCs: (a) complete single cell and segmented channel; (b) boundary conditions with model components; (c) the method for evaluating channel stiffness.

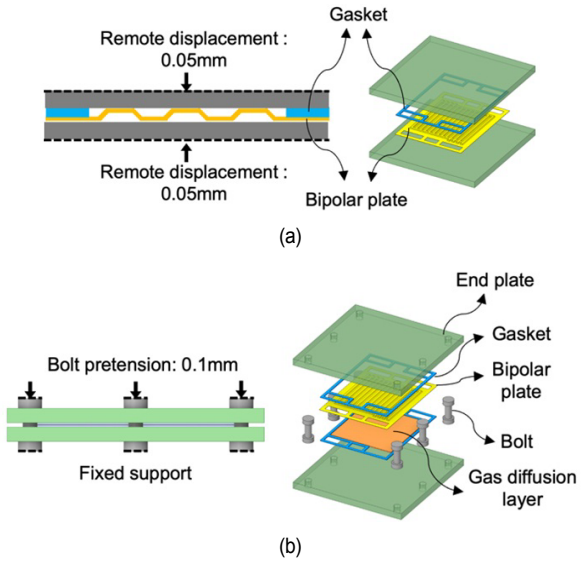

Fig. 4. Schematic of the finite element analysis model for PEMFCs, showing boundary conditions and components, focusing on (a) bipolar plate deformation; (b) GDL compression during cell assembly with bolts.

tions to analyze the deformation of the segmented BP in simulation. Material properties for the structural simulation are listed in Table 2. The boundary conditions were applied to the upper and lower plates, as shown in Fig. 3(b). The endplates were considered as rigid bodies. The contact surfaces between the components were rough, to consider the gaps and avoid sliding. The reaction force was measured to calculate structural stiffness of the channel when the end plates were moved by displacement as the boundary condition.

$$F = k_{channel} \times \Delta x \ . \tag{3}$$

The BP can be modeled as an equivalent stiffness spring, as shown in Fig. 3(c). As expressed in Eq. (3), the equivalent stiffness was calculated using Hooke's law that relates the force applied to the channel to the resulting displacement. For the simulation, the end plate was moved by a constant displacement Δx, and reaction force F was calculated. According to Hooke's law, a larger reaction force corresponds to a higher equivalent structural stiffness because more force is required to achieve the same displacement. Conversely, a high structural stiffness indicates that the channel is less deformable. Therefore, the measured reaction force was used to compare the structural stiffness of different channels.

Fig. 4(a) depicts the components and boundary conditions utilized in the simulation of BP deformation, which was compared to experimental data. Fig. 4(b) illustrates the components and boundary conditions employed in the simulation of bolt assembly, aimed at investigating the influence of BP design on gas diffusion layer (GDL) compression during assembly using bolts.

The computational domains of the FEM model were discretized with tetra-shaped meshes. A mesh size of 0.07 mm and mesh number of approximately 170000 were adopted through a grid dependency test. The average equivalent stress of the BP remained below 5 %.

Table 3. Governing equations used in the CFD simulation for a PEMFC single cell analysis [24].

Governing equation	Mathematical expression
Electron transport	$\nabla(\sigma_{sol}\nabla\phi_{sol}) + R_{sol} = 0$
Protonic transport	$\nabla(\sigma_{mem}\nabla\phi_{mem}) + R_{mem} = 0$
Butler-Volmer equation	$R_{an} = (\zeta_{an} j_{an}^{ref})\left(\frac{[A]}{[A]_{ref}}\right)^{\gamma_{an}}\left(e^{\frac{\alpha_{an}^{an}Fn\eta_{an}}{RT}} - e^{\frac{-\alpha_{cat}^{an}Fn\eta_{an}}{RT}}\right)$ $R_{cat} = (\zeta_{cat} j_{cat}^{ref})\left(\frac{[C]}{[C]_{ref}}\right)^{\gamma_{cat}}\left(e^{\frac{\alpha_{an}^{cat}Fn\eta_{cat}}{RT}} - e^{\frac{-\alpha_{cat}^{cat}Fn\eta_{cat}}{RT}}\right)$
Local surface overpotential	$\eta_{an} = \phi_{sol} - \phi_{mem}$ $\eta_{cat} = \phi_{sol} - \phi_{mem} - V_{oc}$
Mass conservation	$S_{H_2} = -\frac{M_{w,H_2}}{2F} R_{an} < 0$ $S_{O_2} = -\frac{M_{w,O_2}}{4F} R_{cat} < 0$ $S_{H_2O} = -\frac{M_{w,H_2O}}{2F} R_{cat} > 0$
Heat source	$S_h = h_{react} - R_{an,cat}\eta_{an,cat} + I^2 R_{Ohm} + h_L$ $\frac{\partial(\epsilon\rho_l s)}{\partial t} + \nabla\left(\rho_l \frac{Ks^3}{\mu_l}\frac{dp_c}{ds}\nabla s\right) = r_w$
Liquid water formation and transport	$r_w = c_r \max\left(\left[(1-s)\frac{p_{wv} - p_{sat}}{RT} M_{w,H_2O}\right], [-s\rho_l]\right)$ $p_c = \frac{\sigma\cos\theta_c}{\left(\frac{K}{\varepsilon}\right)^{0.5}}\left(1.417(1-s) - 2.12(1-s)^2 + 1.263(1-s)^3\right)$
Gas diffusivity	$D_{eff}^{ij} = \varepsilon^{1.5} D^{ij}$
Electrolyte phase conductivity	$\sigma_{mem} = \beta(0.514\lambda)^w e^{1268\left(\frac{1}{303} - \frac{1}{T}\right)}$
Water content	For a < 1: $\lambda = 0.043 + 17.18a - 39.85a^2 + 36a^3$ For a > 1: $\lambda = 14 + 1.4(a-1)$

2.2 Computational fluid dynamics

Commercial software ANSYS Fluent 2021 R2 PEMFC module was used for the CFD simulation. Fig. 5 shows a schematic of the geometry used in the CFD simulation, including the BPs, end plates, GDL, catalyst layer, and MEA in full size. Two BP shown in Fig. 1, (a) straight and Fig. 1(b) rib-stiffened parallel channels, were used for the simulation. The computational domain was meshed into 4000000 mesh elements, exhibiting less than 7 % variation in the grid independence test.

The governing equations, including the conservation of mass, momentum, energy, species, and charge, are summarized in Table 3. The electrochemical reaction models were based on the anodic and cathodic reactions in the PEMFC. The wall

Table 4. Geometrical and operational parameters applied in the PEMFC CFD simulation.

Parameters	Value
Active area (A_{act})	9 cm^2
GDL thickness	0.4 mm
Membrane thickness	0.05 mm
CL thickness	0.005 mm
Cell open-circuit voltage	1.228 V
H_2 exchange current density	10000 A/m^2
O_2 exchange current density	10 A/m^2
Anode concentration exponent	1
Cathode concentration exponent	1
Anode exchange coefficient	1
Cathode exchange coefficient	1
CL porosity, permeability	0.2, 2e-13 m^2
GDL porosity, permeability	0.36, 5e-12 m^2
Gauge pressure at anode outlets	0
Gauge pressure at cathode outlets	0
H_2 and Air stoichiometry	1.5, 2
Anode and cathode inlet temperature	343.15 K
Anode and cathode inlet RH	100 %/100 %
Reference current density	2 A/cm^2
Area of inlet and outlet	10.2 mm*3 mm

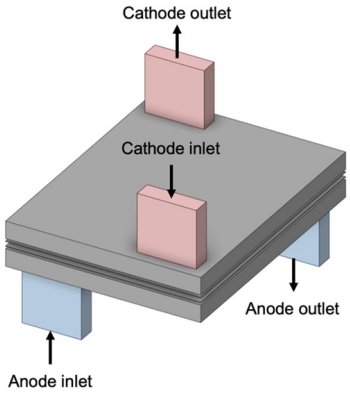

Fig. 5. Geometry of a PEMFC single cell for computational fluid dynamics simulation.

boundary conditions were set to adiabatic, assuming no heat flow to the atmosphere. In addition, an ideal gas mixture, steady-state conditions, laminar flow, isothermal system, incompressible fluid, and isotropic porous zone were assumed for the CFD simulations.

The geometrical and operational parameters of the CFD simulations are listed in Table 4. The inlet velocity was calculated using the parameters for gas flow in the anode and cathode flow fields. The SIMPLE algorithm was used for velocity–pressure coupling. Owing to the laminar flow assumption in the PEMFC, a non-slip boundary condition was used at the wall [25].

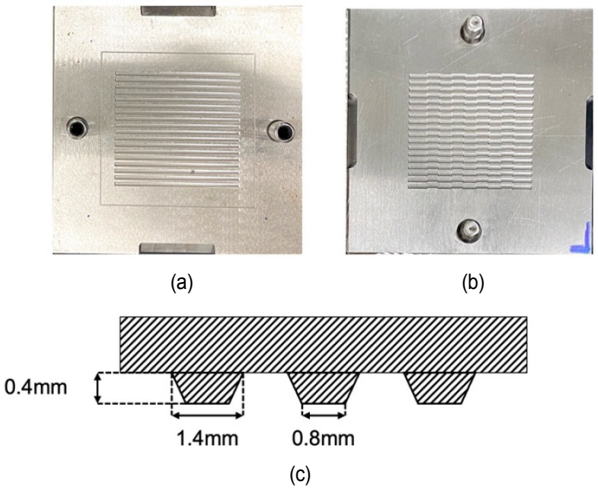

Fig. 6. Upper dies used in structural experiments for the stamping process: photograph of an upper die featuring the (a) straight; (b) rib-stiffened channels; (c) cross-sectional schematic with dimensions.

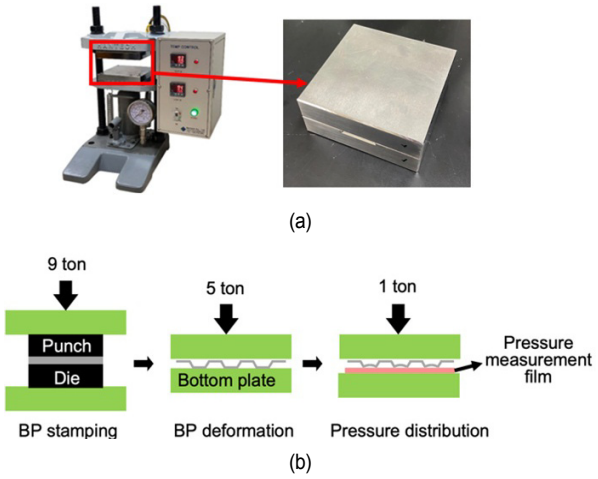

Fig. 7. Experimental setup and procedure for the structural experiment: (a) hydraulic press setup for bipolar plate fabrication; (b) process sequence from stamping to pressure distribution measurement for deformation analysis.

2.3 Experimental procedure

To validate the FEM simulation results, BPs with flow channels were fabricated using a punch and a die. SS304 metal sheets with 0.1 mm thickness were used for the experiments. The straight parallel flow field was formed using the pressing die, as depicted in Fig. 6(a), and the rib-stiffened channel flow field was achieved using the die, as shown in Fig. 6(b). To ensure optimal formability, ribs with a length of 4 mm, distance of 4 mm, height of 0.4 mm, and width of 0.3 mm were incorporated into the die design. Dies are designed to verify the deformation of the flow channels. Hence, only the flow channels were engraved, eliminating the effect of the manifold shape. The geometric dimensions of the punch are shown in Fig. 6(c).

As shown in Fig. 7(a), a hydraulic press was used during the

stamping process to form patterns on the metal sheets. Fig. 7(b) shows the manufacturing process of a BP. First, 9 t of force was applied to the die with a flat metal sheet to fabricate a BP. Subsequently, 5 t of force was applied to the engraved BPs between the rigid plates to induce a deformed channel structure through excessive clamping pressure. To measure the deformation of each plate, the pressure distribution was measured using a pressure-sensitive film (LLW, FUJIFILM Co., Tokyo). The pressure-sensitive film was sandwiched between the bottom plate and the deformed BP. The experimentally measured pressure distributions were compared with FEA simulation results.

To verify the effect of the flow field on fuel cell electrochemical performance, electrochemical experiments were conducted using a single cell configuration. The active area of the single cell was 50 mm by 50 mm, employing straight and rib-stiffened flow field designs for the cathode, depicted in Figs. 2(a) and (b), respectively. The membrane electrode assembly comprised an NR-211 membrane sandwiched between two catalyst layers containing Pt/C (0.4 mg/cm^2, 60 wt%), with gas diffusion layers (carbon papers, SGL 29BB, SIGARET®) of 325 μm thickness utilized on both the anode and cathode sides. The stoichiometry of the anode and cathode was set at 1.2 and 3, respectively, relative to a reference current density of 2.5 A/cm^2. The relative humidity at both the anode and cathode was maintained at 80 %. Chronoamperometry and electrochemical impedance spectroscopy data were collected using a potentiostat at 70 °C and 80 % relative humidity.

3. Results and discussion

3.1 Parametric study of structural analysis in segmented cell

To evaluate the impact of the rib geometry on the mechanical strength, the force required to move the end plates was calculated using the reaction force. First, the influence of the rib height (H) was investigated. The rib height was varied between 0.4 mm and 0.2 mm, while maintaining the other parameters constant at 4 mm length, 4 mm distance, and 0.2 mm width.

Fig. 8 displays the channel cross-section before and after deformation when both channels are compressed by the same displacement. As illustrated in Fig. 8(a), when the rib height was 0.4 mm, same as the channel height, the top surface deformed, whereas the side wall supported the clamping force without deformation. In contrast, at half the rib height, the sidewall deformed and could not support the clamping force as shown in Fig. 8(b). In this case, the equivalent stress on the side walls was low, indicating that the structure cannot withstand the clamping force.

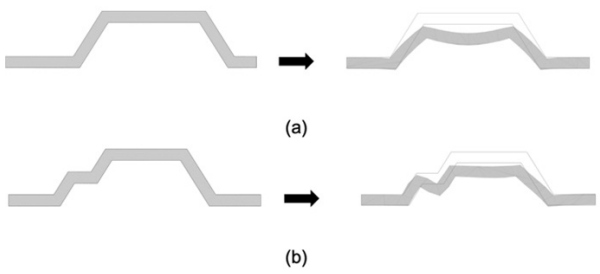

Fig. 8. Cross sections of rib-stiffened channels pre- and post-deformation: with a rib height of (a) 0.4 mm; (b) 0.2 mm, both keeping a rib spacing of 4 mm, rib length of 4 mm, and rib width of 0.2 mm.

Figs. 9(a) and (b) show the through-plane stress contours of the channels with 0.2 mm and 0.4 mm height ribs, respectively. As shown in Fig. 9(a), when the rib height was half the channel height, the entire channel deformed instead of supporting the clamping force. The deformed channels did not support the clamping force. Hence, the reaction force calculated from the simulation results is 44031 N for the 0.2 mm height and 59621 N for the 0.4 mm height.

The initial parametric study noted that a smaller rib height negatively affected the structural stiffness. Consequently, for subsequent simulations, the rib height was fixed at 0.4 mm, equal to the channel height. The second parameter was the number of ribs that were varied by adjusting the distance and length of the ribs. Specifically, the length and distance of the ribs were set at 4 mm for five ribs and 3 mm for seven ribs, while maintaining the width constant at 0.3 mm. As shown in Fig. 10, a larger reaction force was achieved by increasing the number of ribs of the same size. The edge walls of the ribs served as

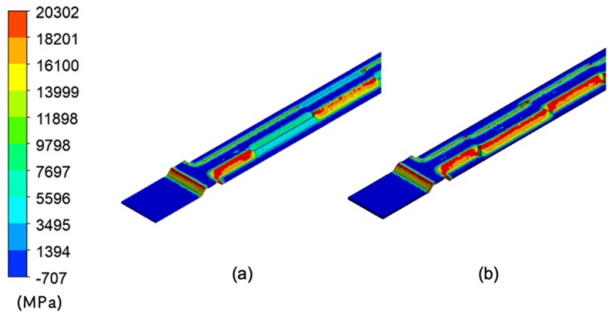

Fig. 9. Through-plane stress distribution in rib-stiffened channels with a rib height of (a) 0.2 mm; (b) 0.4 mm.

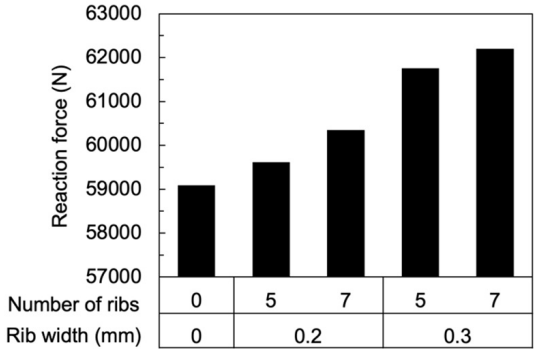

Fig. 10. Reaction force in relation to variations in the rib width and number of ribs, with changes in the rib width, length, and distance.

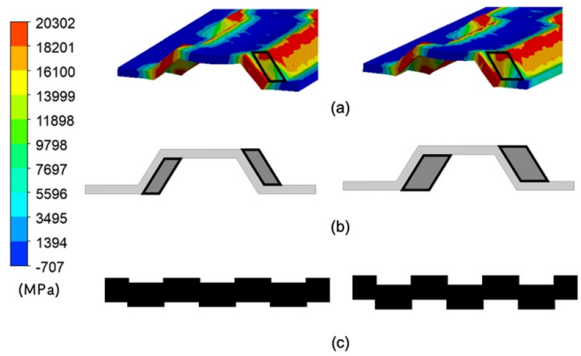

Fig. 11. (a) Through-plane stress contours; (b) cross-sectional shapes; (c) top surface schematics of 0.2 mm (left) and 0.3 mm (right) rib widths.

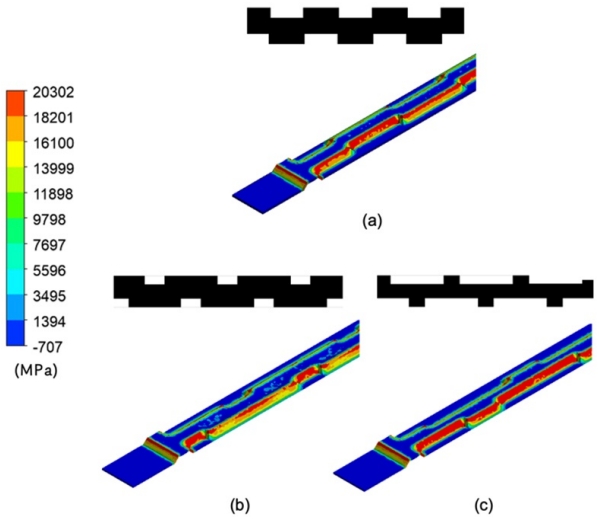

Fig. 12. Through-plane stress distributions and channel top surface schematics for varying rib-stiffened channels: (a) length 4 mm, distance 4 mm; (b) length 2 mm, distance 6 mm; (c) length 6 mm, distance 2 mm.

supporting columns, providing resistance to the applied force, and exhibiting reduced deformation.

Another parameter to consider is the width, which determines the distance of shift from the original position. Channels with a width of 0.3 mm, as depicted in Fig. 10, resulted in a greater reaction force. Fig. 11(a) demonstrates how the wall on the rib supports enhances pressure strength. Additionally, Fig. 11(b) displays the undeformed shape of rib-stiffened channels, while Fig. 11(c) provides schematics of the channel top surface, highlighting wider walls on ribs with a 0.3 mm width. The increased width of the columns amplifies the supporting force, consequently leading to a higher reaction force, as observed in Fig. 10. The supportive columns on the side walls significantly contribute to the overall stiffness of the channel structure, thereby enhancing its structural stability. Moreover, it is noteworthy that an increased number of ribs and wider ribs results in more rib walls, as well as an amplified reaction force and structural strength. The greater number and width of ribs contributes to a more robust support system, further enhancing the overall stability and performance of the channel structure.

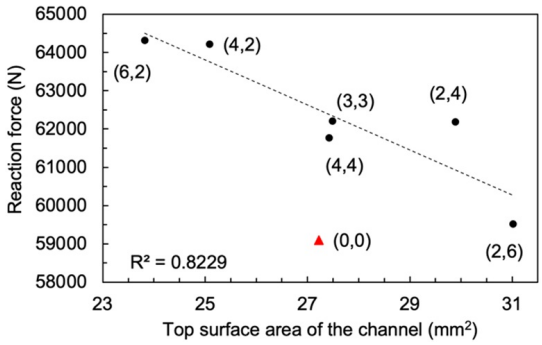

Fig. 13. Correlation between top surface area and reaction force with varying rib-stiffened channels (black dot) and straight channel (red triangle).

The last parameter to consider is the ratio of the rib length to the distance. While the number of ribs remained constant and the number of ribs acting as supporting columns remained the same, the top surface area of the channel varied. This variation in top surface area with varying length and distance ratio, along with the through-plane stress, is illustrated in Fig. 12. Notably, the channel with a length of 2 mm and a distance of 6 mm exhibits the largest top surface area, whereas the channel with a length of 6 mm and a distance of 2 mm has the smallest top surface area. It is observed that the top surface area of the channel decreases as the rib length-to-distance ratio decreases.

As demonstrated in Fig. 13, the reaction force tends to increase as the top surface area decreases. When the top surface area of the channel is large, deformation occurs on the channel, and the side wall cannot fully resist the applied force. This is evidenced by smaller through-plane stress on the wall detected in larger top surface areas, as shown in Fig. 12(b). Conversely, when the length-to-distance ratio is increased, the top surface area becomes narrower, resulting in relatively small deformation, and the side walls effectively resist the clamping force. This is evident from the higher through-plane stress on the wall with a smaller top surface area, as illustrated in Fig. 12(c).

A smaller top surface area is less deformable and better resists the clamping force. This structural strength allows for a reduction in the thickness of the BP. Comparing a straight channel with a thickness of 0.1 mm that resulted in a reaction force of 59093 N with a rib-stiffened channel with a length of 6 mm, distance of 2 mm, and thickness of 0.92 mm that resulted in a reaction force of 59263 N, evidently, the reaction forces were nearly the same. The overall weight of the fuel cell stack could be significantly reduced using a rib-stiffened channel design. Utilizing the rib-stiffened channel design results in an 8 % reduction in BP weight. If assuming a 5 kW/kg stack, the weight reduction could lead to an increase in power density to 5.4 kW/kg.

3.2 Structural analysis and experimental validation of bipolar plate deformation

Full-scale straight and reinforced parallel flow-field patterns

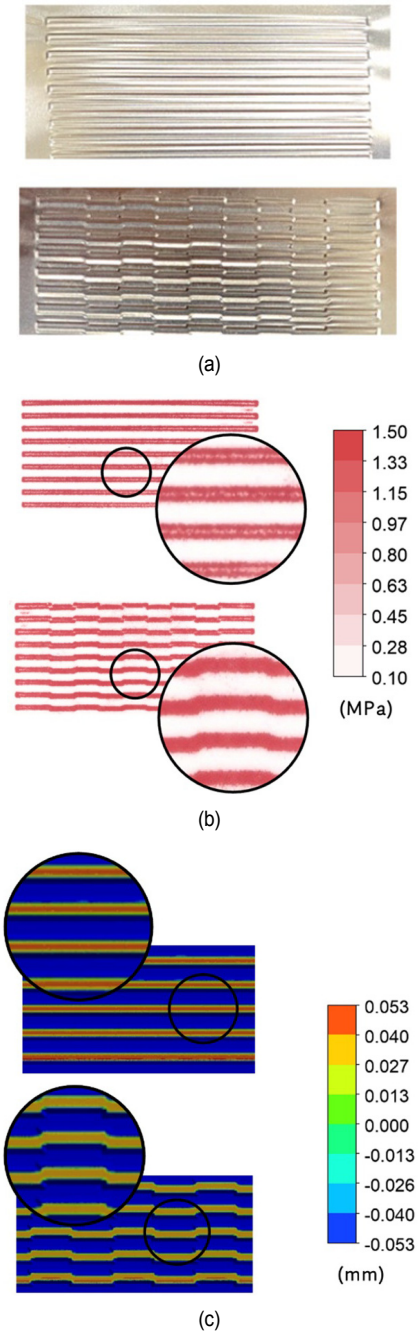

Fig. 14. Comparison of simulation and experimental results for full-scale bipolar plates: (a) fabricated plates after deformation; (b) pressure distribution analysis of deformed plates using a pressure-sensitive film; (c) results from computer simulations depicting through-plane deformation using straight (top) and rib-stiffened (bottom) channels.

were formed using a hydraulic press. The reinforced flow field had ribs with a height of 0.4 mm, length of 3 mm, distance of 3 mm, and width of 0.3 mm, exhibiting a higher reaction force than the straight parallel flow field. Fig. 14 compares the straight and reinforced parallel flow fields through simulations and experiments. Fig. 14(a) shows the deformed shape of the BPs after pressing with a 5 t force. Fig. 14(b) illustrates the

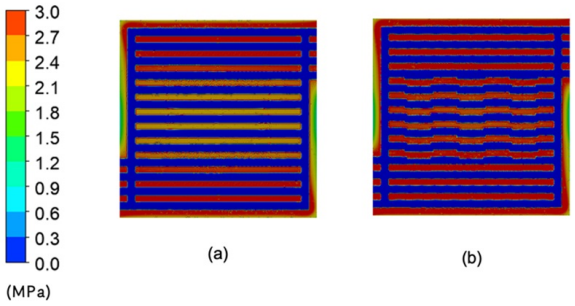

Fig. 15. Through-plane stress distribution in gas diffusion layers with (a) straight; (b) combined straight and rib-stiffened channels.

pressure distribution of the deformed BPs, where red indicates high pressure and white denotes low pressure. Fig. 14(c) shows the simulation results for the through-plane deformation of the BPs. In straight channels, a white line appears at the center of the channel because of top surface deformation. The pressure distribution in the experimental data is in good agreement with the simulation results. The deformation contour from the full-scale structural analysis reveals that the center of the straight channels appears orange, indicating high deformation, whereas the reinforced channels appear yellow, indicating less deformation. In the case of the reinforced BP, the ribs act as a support, leading to a reduced deformation on the top surface area.

3.3 Gas diffusion layer compression

The impact of BP flow field design on GDL compression after cell assembly was investigated through structural analysis. Pressure distribution on the GDL was compared by measuring through-plane stresses on the GDL's surface in contact with the BP. In Fig. 15(a), through-plane stress on the GDL's surface is shown when using a straight flow field, while Fig. 15(b) displays stress when using a combined flow field.

With straight flow field, the center exhibits less compression, as indicated by the yellow color. This is attributed to the end plate bending when bolts are fastened, resulting in greater pressure on the edges and less on the center. In contrast, the combined flow field, featuring rib-stiffened channels, not only mitigates end plate deformation but also efficiently transfers clamping pressure to the GDL.

Contact resistance occurs at the interface where the rib meets the GDL. Average through-plane stress and standard deviation were compared in areas with stress exceeding 0.2 MPa. For the straight flow field, the average through-plane stress is 0.97 MPa, with a standard deviation of 0.35 MPa. In contrast, for the combined flow field, these values are 1.04 MPa and 0.32 MPa, respectively. Using the combined flow field results in an increased average through-plane stress and a reduced standard deviation because the center region is sufficiently compressed. Excessive compression can damage the GDL's microstructure, while insufficient compression can increase contact resistance, degrading fuel cell performance.

Therefore, achieving uniform compression of the GDL enhances fuel cell performance by reducing contact resistance.

3.4 Electrochemical reaction simulations and experimental validation

A CFD analysis and electrochemical experiments were conducted to investigate the influence of the rib structure on electrochemical performance. While rib structures are intended to enhance structural strength, their potential impact on electrochemical performance requires careful consideration. Fig. 16 illustrates the polarization curves obtained from the fluid simulation and electrochemical experiments using straight and rib-stiffened channels. Fig. 16(a) depicts the current density-voltage curve, and Fig. 16(b) presents impedance spectroscopy data at 0.4 V operation. Similar current densities were observed between rib-stiffened and straight flow fields at high voltage operation, while the rib-stiffened flow field demonstrates superior performance with higher current densities at low voltage operation, consistent with the simulation results. Discrepancies between experimental and simulation results arise from the presence of liquid water. In the simulation, hydrogen, oxygen, and water were all assumed to be in a single gas phase. Fig. 16(b) is a Nyquist plot analyzing the resistance at 0.4 V operation. The high-frequency region shows comparable ohmic resistance, while the low-frequency region indicates that the rib-stiffened configuration exhibits reduced mass transport resistance. Consequently, the staggered configuration of the rib-stiffened channel facilitates water discharge and reactant supply, leading to enhanced performance at high current densities, signifying a reduction in mass transport resistance in fuel cells.

Fig. 17 illustrates fluid velocity vectors at 0.4 V, contrasting

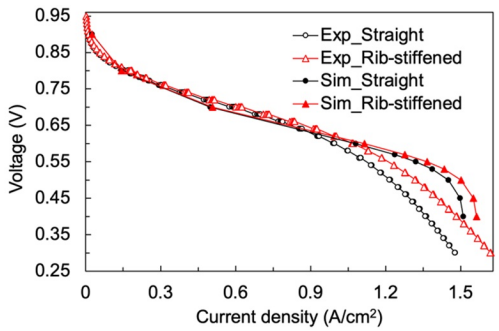

(a)

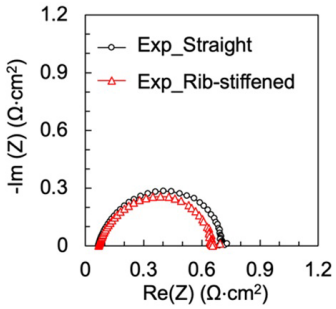

(b)

Fig. 16. Electrochemical characterization of PEMFC single cells with (a) current density – voltage curve comparing simulation and experimental results; (b) experimental impedance spectroscopy data at 0.4 V using rib-stiffened and straight flow fields.

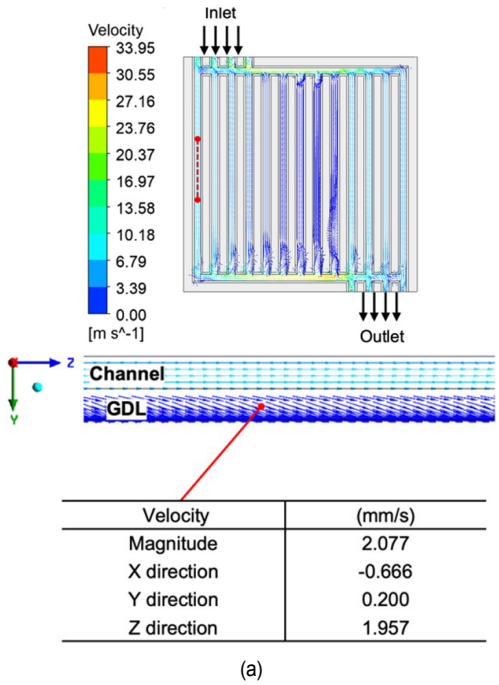

Velocity	(mm/s)
Magnitude	2.077
X direction	-0.666
Y direction	0.200
Z direction	1.957

(a)

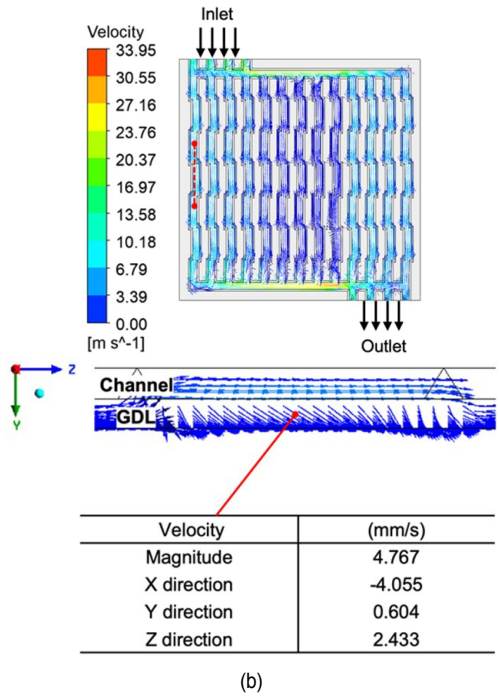

Velocity	(mm/s)
Magnitude	4.767
X direction	-4.055
Y direction	0.604
Z direction	2.433

(b)

Fig. 17. Computational fluid dynamics results depicting fluid velocity vectors in the cathode channel (top), cross-sectional velocity vectors with gas diffusion layer (middle), and detailed velocity components (bottom) for (a) straight; (b) rib-stiffened channels.

(a) straight channels and (b) rib-stiffened channels. At the top, it presents the velocity vector within the channel. In the middle, the velocity vector is visualized within the cross-section outlined by the red dotted line in Fig. 17(a), encompassing both the channel and GDL. Finally, detailed velocity components in the GDL are depicted at the bottom. In rib-stiffened channels, flow is obstructed by rib walls, altering the flow direction. Cross-sectional analysis reveals minimal channel-to-GDL flow in straight channels, whereas rib-stiffened channels exhibit flow vectors directed towards the GDL. Notably, the overall flow magnitude within the GDL is approximately twice as large, with the Y-direction component (aligned with the catalyst) increasing from 0.2 to 0.604 and the x-direction component (in-plane) rising from 0.666 to 4.055. These observations indicate improved reactant transport even beneath the ribs, resulting in effective reduction of oxygen transfer resistance and decreased mass transport overpotential.

4. Conclusions

To enhance the structural strength of fuel cells in automotive applications, a stiffened rib channel was integrated into a metal bipolar plate (BP) design. Through a parametric study, variations in rib height, width, length, and distance were explored to optimize rib shape. A higher reaction force, achieved when clamping the BP with the same displacement, indicated a stronger structure. The results of the parametric study reveal that an increased number of ribs with wider widths enhances the structural stiffness of the channel, resulting in heightened reaction forces. Additionally, the ratio of rib length to distance influences the top surface area of the channel; a larger length-to-distance ratio leads to a smaller top surface area and reduced deformability. Consequently, the reinforced flow field with ribs exhibited greater strength compared to the straight flow field. This also implies the potential for achieving the same structural stiffness with a thinner and lighter bipolar plate. Simulation results demonstrated that a 0.92 mm rib-stiffened bipolar plate exhibits a similar reaction force to a 1 mm straight bipolar plate, resulting in an 8 % reduction in BP weight.

Flow analysis and experimental results indicated that adopting a structurally reinforced flow field improves fuel cell performance. The presence of ribbed walls alters flow direction, inducing airflow in the gas diffusion layer (GDL) and thereby reducing mass transfer overpotential. Consequently, current density becomes more uniform, leading to enhanced performance. Structurally reinforced metal BPs effectively mitigate channel deformation, resulting in improved fuel cell performance.

Acknowledgments

This work was supported by Korea Evaluation Institute of Industrial Technology (20009835 and RS-2022-00156525) and Korea Institute of Energy Technology Evaluation and Planning (20203010030010).

References

[1] UNFCCC, *The Paris Agreement. What is the Paris Agreement?*, UNFCCC (2015) https://unfccc.int/process-and-meetings/the-paris-agreement, Accessed on August 7, 2023.

[2] G. J. Offer et al., Comparative analysis of battery electric, hydrogen fuel cell and hybrid vehicles in a future sustainable road transport system, *Energy Policy,* 38 (1) (2010) 24-29.

[3] B. Cárdenas et al., Short-, medium-, and long-duration energy storage in a 100% renewable electricity grid: a UK case study, *Energies,* 14 (24) (2021) 8524.

[4] B. Wu, M. Matian and G. J. Offer, Hydrogen PEMFC system for automotive applications, *International J. of Low-Carbon Technologies,* 7 (1) (2012) 28-37.

[5] A. Tang et al., An overview of bipolar plates in proton exchange membrane fuel cells, *J. of Renewable and Sustainable Energy,* 13 (2) (2021) 022701.

[6] J. Hamelin et al., Dynamic behavior of a PEM fuel cell stack for stationary applications, *International J. of Hydrogen Energy,* 26 (6) (2001) 625-629.

[7] H. C. Kuan et al., Preparation, electrical, mechanical and thermal properties of composite bipolar plate for a fuel cell, *J. of Power Sources,* 134 (1) (2004) 7-17.

[8] S. Karimi et al., A review of metallic bipolar plates for proton exchange membrane fuel cells materials and fabrication methods, *Advances in Materials Science and Engineering,* 2012 (2012).

[9] A. M. Dafalla and F. Jiang, Stresses and their impacts on proton exchange membrane fuel cells a review, *International J. of Hydrogen Energy,* 43 (4) (2018) 2327-2348.

[10] H. N. Yu, S. S. Kim and J. Do Suh, Composite endplates with pre-curvature for PEMFC (polymer electrolyte membrane fuel cell), *Composite Structures,* 92 (6) (2010) 1498-1503.

[11] P. Lin, P. Zhou and C. W. Wu, Multi-objective topology optimization of end plates of proton exchange membrane fuel cell stacks, *J. of Power Sources,* 196 (3) (2011) 1222-1228.

[12] C. K. Jin, M. G. Jung and C. G. Kang, Fabrication of aluminum bipolar plates by semi - solid forging process and performance test of TiN coated aluminum bipolar plates, *Fuel Cells,* 14 (4) (2014) 551-560.

[13] R. N. Lakshmi, Forming of ferritic stainless steel bipolar plates, *Ph.D. Thesis*, University of Windsor, Canada (2012).

[14] B. Jang, J. Lee and S. Kwon, Design and fabrication of fully enclosed micro PEM fuel cell using novel glass bipolar plates, *POWERMEMS 2010, The 10th international workshop on Micro and Nanotechnology for Power Generation and Energy Conversion Applications,* Leuven, Belgium (2010).

[15] D. Moreno et al., ESR dating of Middle Pleistocene archaeo-paleontological sites from the Manzanares and Jarama river valleys (Madrid basin, Spain), *Quaternary International,* 520 (2019) 23-38.

[16] Z. Wu et al., An inner-field uniform pressure actuator with high performance and its application to titanium bipolar plate forming, *International J. of Machine Tools and Manufacture,* 155 (2020) 103570.

[17] H. Zhu et al., Evolution of Ti2Ni precipitations during annealing and their effects on properties of Ti–Nb–Ni foil as PEMFC bipolar plates substrate, *International J. of Hydrogen Energy,* 48 (39) (2023) 14822-14836.
[18] D. Qiu et al., Study on shape error effect of metallic bipolar plate on the GDL contact pressure distribution in proton exchange membrane fuel cell, *International J. of Hydrogen Energy,* 38 (16) (2013) 6762-6772.
[19] D. Qiu et al., A micro contact model for electrical contact resistance prediction between roughness surface and carbon fiber paper, *International J. of Mechanical Sciences,* 124 (2017) 37-47.
[20] P. Yi et al., Performance of a proton exchange membrane fuel cell stack using conductive amorphous carbon-coated 304 stainless steel bipolar plates, *J. of Power Sources,* 195 (20) (2010) 7061-7066.
[21] ANSYS, Inc., *Ansys® Mechanical, Release 2020R1, Engineering Data*, ANSYS, Inc. (2020).
[22] Z. Jie and Y. Hu, Sealing performance and mechanical behavior of PEMFCs sealing system based on thermodynamic coupling, *International J. of Hydrogen Energy,* 45 (43) (2020) 23480-23489.
[23] SGL Group, *GDL 24 & 25 Series Gas Diffusion Layer*, SGL Group, Germany (2007).
[24] ANSYS, Inc., *Ansys® Fluent, Release 2020R1, Help System, Modeling Fuel Cells*, ANSYS, Inc (2020).
[25] Y. Al-Okbi et al., Influence of design anode and cathode channel on (PEMFC) fuel cell performance, *Materials Today: Proceedings,* 42 (2021) 2177-2184.

Choeun Kim is a research fellow at the Institute of Engineering at the University of Seoul, Korea. She received her Master's in Mechanical and Information Engineering from the University of Seoul. Her research interests include the analysis of electrochemical devices, such as fuel cells and electrolysis, using computational fluid dynamics, finite element analysis, and electrochemical experiments.

Seoungsu Im is a research fellow at the Institute of Engineering at the University of Seoul, Korea. He received his Master's in Mechanical and Information Engineering from the University of Seoul. His research interests include the analysis of electrochemical devices, such as fuel cells and electrolysis, using computational fluid dynamics.

Youngseung Na is an Associate Professor of Mechanical and Information Engineering at the University of Seoul, Korea. He received his Dr.-Ing. degree in Mechanical Engineering from TU Braunschweig and International Max Planck Research School, Germany. His research interests include electrochemical systems such as fuel cells, electrolyzers, and electrochemical hydrogen compressors.